International Journal of Multiphase Flow 34 (2008) 1152–1160

Contents lists available at ScienceDirect

International Journal of Multiphase Flow

journal homepage: www.elsevier.com/locate/ijmulflow

# A method for characterising solids translational and rotational motions using Multiple-Positron Emission Particle Tracking (Multiple-PEPT)

Z. Yang [a,b], X. Fan [a], S. Bakalis [b], D.J. Parker [a], P.J. Fryer [b,*]

[a] School of Physics and Astronomy, University of Birmingham, Birmingham B15 2TT, UK
[b] Department of Chemical Engineering, School of Engineering, University of Birmingham, Birmingham B15 2TT, UK

ARTICLE INFO

*Article history:*
Received 7 February 2008
Received in revised form 2 June 2008
Accepted 10 June 2008
Available online 24 June 2008

*Keywords:*
Multiple-Positron Emission Particle Tracking
Location algorithm
Multiphase flow
Particle rotation
Rotation reconstruction

ABSTRACT

Solid motion can be classified into translational motion and rotational motion; both play an important role in a wide range of engineering processes. While translational motion has been extensively studied in various systems, there is a lack of information on rotational motion, possibly due to a lack of appropriate experimental techniques. For a number of mixing processes involving heat transfer for solid–liquid mixtures, the heat transfer coefficient between solid and liquid is critical in determining process times and overall product characteristics, and is greatly dependent on both rotational and translational behaviours of the solids, which ideally need to be studied simultaneously. This paper presents a new technique, Multiple-Positron Emission Particle Tracking (Multiple-PEPT), which can follow multiple particles simultaneously through a considerable thickness of surrounding material. Both translational and rotational motions of the solid can be reconstructed. The accuracy of the method for the translational velocity was better than 10% while for the angular velocity 23% for speeds up to 0.25 m/s. Multiple-PEPT will therefore offer the possibility to study translational and rotational motions for a range of engineering systems. The potential applications of tracking solid translational and rotational motions are illustrated by an example of tracking a cubed potato in a rotating can.



## 1. Introduction

### 1.1. Importance of solid–liquid flows

Solids motions play an important role in a wide range of engineering processes. For example, a number of food processing problems involve the transport and thermal processing of solid–liquid mixtures (Lareo et al., 1997a,b; Barigou et al., 2003). Particles are usually large (on the order of 1–2 cm) and in high solids fractions (up to 50%), suspended in viscous and non-Newtonian fluids, where the density of the particles and liquids is similar. Flow is normally carried out whilst the material is being heated or cooled; both in batch systems (such as the sterilization of canned food) or in continuous flows through pasteurizers and sterilizers. The flow of single particles is complex; for example, Lareo et al. (1997a,b) show that particle radial migration can occur.

Liu et al. (1993) describe experimental work using metal detectors to identify particle translational velocities, and Fairhurst et al. (2001) use single-tracer PEPT to follow particles in high solids fraction flows showing the presence of capsule flows of high velocity. Both translational and rotational motions are however important in processing of these materials:

- *Translational flow*. Translational flow controls the residence time of solids in the process. For example, heat exchangers are commonly designed assuming that the fastest particle can travel twice as fast as the mean;
- *Rotational flow*. Rotational flow is significant in defining the interphase heat transfer coefficients which may control the particle heating and cooling rates (Mankad et al., 1995, 1997; Mankad and Fryer, 1997).

Characterisation of solids motion has been studied in a variety of systems, for instance, visualization of circulating fluidized beds (Horio and Kuroki, 1994); mixing studies in drums (Santomaso et al., 2004, 2005), granular flow and segregation in four-bladed mixer by Conway et al. (2005); and solids motion studies in fluidized beds by Gera et al. (1998) and Werther (1999). All these focus on the translational motion of the solids alone.

A number of studies have also considered solids rotation; for example, Duchanoy et al. (2003) consider the lift force produced by solids rotation on the particle tracks. In some gas–solid flows, lift is significant, for example, in the flow of pulverized coal (Hussainov et al., 1996). The distribution of solids and flow field are also affected by solid rotation. Some theoretical and numerical investigations have been reported to show the effects of solid rotation on gas–solid and liquid–solid two-phase flow (Goldschmidt et al., 2004; You et al., 2001), and heat transfer (Wang et al., 1989). Wang

* Corresponding author. Tel.: +44 121 414 5451; fax: +44 121 414 5377.
*E-mail address:* p.j.fryer@bham.ac.uk (P.J. Fryer).

0301-9322/$ - see front matter © 2008 Elsevier Ltd. All rights reserved.
doi:10.1016/j.ijmultiphaseflow.2008.06.002

et al. (1989) examined the case of a rotating solid sphere in a stationary medium with a uniform temperature gradient, and then noted that a solid rotating in this gradient absorbs heat from the hot fluid and rejects it on the cold side. Solid rotation thus improves the internal energy transport in much the same way as increasing the solid's thermal conductivity. The rotating solid transports heat at a rate proportional to the rotational velocity. The rotational motion of solids also enhances slip which is related to the heat transfer (Mankad et al., 1995).

Most of the previous rotation studies focused on solid rotation by means of high-speed photography (Tsuji et al., 1985; White and Schulz, 1977; White, 1982; Lee and Hsu, 1996) using a stroboscope. The solids used were marked with some special lines or spots on their surfaces in advance, so rotation speeds could be recognized easily. Kale et al. (1989) presented a method based on Laser Doppler system. However, optical tracking techniques are necessarily limited to transparent systems and have resolution limited by refraction. Similar, transparency is needed to use methods such as particle imagery velocimetry (PIV) (Duursma et al., 2001). Magnetic resonance imaging has also been used to study two-phase flows, but this requires the system to be metal free (Reyes et al., 1998). Other tomographic studies have been made on the dynamics of solids in multiphase flows. Bhusarapu et al. (2007) use radioactive tracers to study circulating fluidised beds, and identify differences in the behaviour between the fast fluidised and dilute phase transport flows, whilst Razzak et al. (2007) use electrical resistance tomography to study these flows.

### 1.2. Use of Positron Emission Particle Tracking (PEPT)

Positron Emission Particle Tracking (PEPT) was developed at the University of Birmingham for tracking a single particle accurately and non-invasively for various applications in engineering and science (Parker et al., 1993, 1996, 1997a,b, 2002). The technique involves a positron camera, a labelled tracer particle (Fan et al., 2006a,b), and a location algorithm used for calculating the tracer location and speed. The camera consists of two position-sensitive detectors, each with an active area of $500 \times 400\ mm^2$, mounted on either side of the field of view, and is used to detect pairs of 511 keV $\gamma$-rays. The tracer particle is labelled with a radionuclide which decays by $\beta^+$ decay with the emission of a positron. Each positron rapidly annihilates with an electron, giving rise to a pair of 511 keV $\gamma$-rays which are emitted almost exactly back-to-back. The two $\gamma$-rays are simultaneously detected in the two detectors and define a trajectory passing close to the source, as shown in Fig. 1. The location algorithm is used to minimize the sum of perpendicular distances to the various trajectories. From successive locations, the velocity of the labelled particle can be found as it passes through the view of the camera (Parker et al., 1996, 1997a,b, 2002; Bakalis et al., 2006). PEPT has been used widely to study solid flows (such as fluid beds; Fan et al., 2008a,b) as well as the behaviour of liquids (where the tracer particle has to be chosen to be isokinetic with the fluid, see Bakalis et al., 2006).

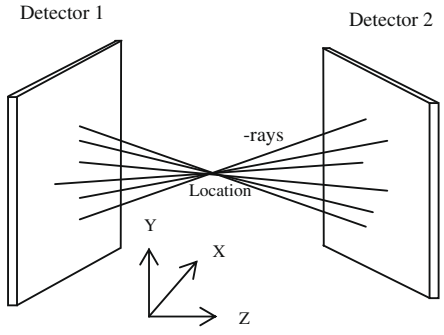


**Fig. 1.** Schematic diagram of PEPT for single particle.

This technique has been recently further improved to track multiple particles by Yang et al. (2006, 2007a,b). The initial applications of the work were in the study of two separate particles. The method has been shown to be efficient for two separate particles and up to three particles attached to a single particle. In this paper, the Multiple-PEPT method is used to follow solids motions in both directions of translational and rotation through tracking three tracer particles, mounted on the surface of a solid. Reconstruction of translational and rotational motions has been validated through tracking three moving particles mounted on a rotating cube.

The method has a range of potential applications. We have demonstrated its possible uses here using the simple case of a cubed potato in a rotating can. The method can be used to track a range of motions of the solid as a function of the type of process variables found in the food industry.

## 2. Multiple-PEPT technique

The Multiple-PEPT technique is developed based on PEPT (Parker et al., 1993) which can follow the motion of a single radioactive tracer. To track multiple particles, the tracers are labelled at different levels of radioactivity. For a given set of events, most $\gamma$-rays originate from the tracer with the strongest radioactivity. Thus, the most active tracer can be located by using the single PEPT algorithm while the trajectories from the remaining tracers are regarded as corrupt trajectories. The trajectories used for the location of the strongest tracer are then removed from the subset. The locations of the second and the third tracers are then calculated in a similar way. The following briefly describes the algorithm for tracking multiple particles. Details of the technique and the algorithms developed for the tracer location can be found in Yang et al. (2006).

For a selected set S of sequential trajectories $L_1, \ldots, L_N$ which are recorded as data from the camera, the sum of distances from any point $(x,y,z)$ to the $\gamma$-ray trajectories can be stated as follows:

$$D_s(x,y,z) = \sum_s \delta_i(x,y,z) \tag{1}$$

where $\delta_i(x,y,z)$ is the distance of the $i$th trajectory from the point $(x,y,z)$.

To get the minimum sum of distances, the minimum solution must be obtained by

$$\begin{cases} \frac{\partial D_s(x,y,z)}{\partial x} = 0 \\ \frac{\partial D_s(x,y,z)}{\partial y} = 0 \\ \frac{\partial D_s(x,y,z)}{\partial z} = 0 \end{cases} \tag{2}$$

From Eq. (2), the minimum distance point $(x_0,y_0,z_0)$ can be obtained as the first approximation. The mean deviation of these trajectories from the minimum distance point is then

$$d_s(x_0,y_0,z_0) = D_s(x_0,y_0,z_0)/N(S) \tag{3}$$

where $N(S)$ is the number of events in the set $S$.

The distance $\delta_i(x_0,y_0,z_0)$ of the $i$th trajectory from the point $(x_0,y_0,z_0)$ is calculated for a given set of trajectories. The trajectories for which $\delta_i(x_0,y_0,z_0)$ is larger than $kd_s(x_0,y_0,z_0)$ are discarded, where $k$ is a fixed parameter. This leaves a subset $S_1$ of events and a new (smaller) mean deviation $d_{s1}(x_1,y_1,z_1)$, from which an improved location $(x_1,y_1,z_1)$ of the strongest tracer is calculated. The algorithm proceeds until only a specified fraction $f$ of the initial trajectories remains, i.e. terminates at step $n$, where $N(S_n) = fN(S)$.

The parameter $k$ determines the rate at which trajectories are discarded. Values of $k$ between 1 and 1.5 have been investigated.

The optimum lies somewhere between these two extremes (Parker et al., 1993).

If the parameters $f_1, f_2$ and $f_3$ are defined as the first-, second- and third-tracer fractions of the initial trajectories, respectively, and another parameter $\rho$ as the fraction of the desired trajectories in the entire original set $S$, the specified fraction $f$ of the initial trajectories is equal to $\rho f_1$. The parameter $\rho$ has been investigated, and its optimum value lies between 0.20 and 0.33 (Parker et al., 1993).

After the strongest tracer is located, trajectories passing close to the located tracer are then removed from the dataset. In a similar way, repeating the above procedure, the locations of the second and the third tracers are then calculated.

The amount of $\gamma$-rays is recalculated around each located tracer for the entire original set $S$ of trajectories to make sure the first, second and third highest amount of $\gamma$-rays around the tracers correspond to the first, second and third strongest tracers, respectively.

The final outcome is that the subsets $S_{F1}$, $S_{F2}$ and $S_{F3}$ of trajectories are selected from the original set, from which the locations of Particles 1, 2 and 3 are calculated as their minimum distance points $(x_{F1},y_{F1},z_{F1})$, $(x_{F2},y_{F2},z_{F2})$ and $(x_{F3},y_{F3},z_{F3})$, respectively, during the time interval covered by these subsets. Each event $L_i$ has its time of measurement $t_i$ recorded, and the location thus arrived at is considered to represent the particles' position at time

$$t = \frac{1}{N_F}\sum_{S_F} t_i \tag{4}$$

where $N_F \equiv N(S_F)$ is the number of trajectories in the final subset, and $S_F = S_{F1} \cup S_{F2} \cup S_{F3}$.

Having located the particles once, the new set starts immediately after trajectories have been discarded in the previous set.

## 3. Translational and rotational motions

For any regular shape, the translational and rotational motions can be reconstructed by tracking 3 particles if the positions of the particle are well designed. Here we show one typical example, for tracking a cube. The best way to reconstruct the solid translational and rotational motions easily in a three-dimensional space is

(i) to place two tracers at the ends ($a + b$) of any side
(ii) and another at any opposite corner ($c$),

so that the line $ac$ goes through the centre of mass $m$. This is shown in Fig. 2A.

### 3.1. Reconstruction of translational motion

Yang et al. (2006) show that the estimated cube side from Multiple-PEPT has a very small error (less than 2.9%). This indicates that the Multiple-PEPT could be used to reconstruct the cube. To obtain the locations of the cube precisely, a known cube is used to fit the experimental locations as follows.

If the length of a side of the cube is $S$, the following equations can be obtained from Fig. 2A and the geometry of the system:

$$|\vec{am}| = |\vec{bm}| = |\vec{cm}| = \frac{\sqrt{3}}{2}S \tag{5}$$

Thus the function

$$\left(|\vec{bm}| - \frac{\sqrt{3}}{2}S\right)^2 + \left(|\vec{am}| - \frac{\sqrt{3}}{2}S\right)^2 + \left(|\vec{cm}| - \frac{\sqrt{3}}{2}S\right)^2 \tag{6}$$

will equal zero if the distances are correctly found by the algorithm. Therefore, a function of $\vec{m}$ is defined,

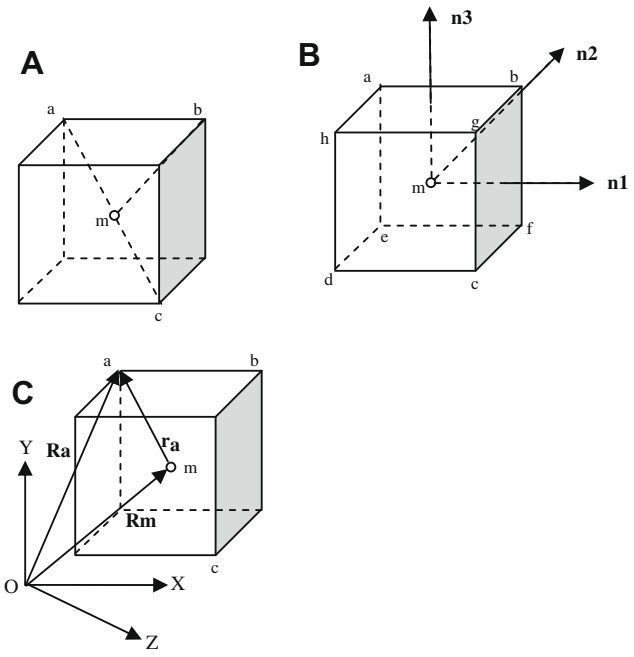


**Fig. 2.** Geometry of the labelled solid in three-dimensional space. (A) the construction of the centre of the cube, (B) the construction of the cube, (C) coordinate scheme for the solid rotation of a rigid body.

$$y = f(\vec{m}) \equiv \left(|\vec{bm}| - \frac{\sqrt{3}}{2}S\right)^2 + \left(|\vec{am}| - \frac{\sqrt{3}}{2}S\right)^2 + \left(|\vec{cm}| - \frac{\sqrt{3}}{2}S\right)^2 \tag{7}$$

so by minimization of the $f(\vec{m})$, the centre of the cube can be identified. By tracking the three tracer positions at the corners a, b and c, respectively, the motion of the centre of the cube $m$ can be found. This represents the solid translational motion.

### 3.2. Reconstruction of rotation

Reconstruction of rotation round the centre of the cube is possible from the change in the relative position of the three tracers. Let $a$, $b$, $c$, $d$, $e$, $f$, $g$ and $h$ are vertexes of the cube, so that **n1**, **n2** and **n3** are normal vectors to the planes $bgcf$, $abfe$ and $ahgb$, respectively, and $m$ is the centre of the cube as described above; this geometry is shown in Fig. 2B.

The three vectors are perpendicular to each other, so:

$$\mathbf{n3} = \mathbf{n1} \times \mathbf{n2} \tag{8}$$

$$\mathbf{n1} \bullet \mathbf{n2} = 0 \tag{9}$$

Then the location of each of the tracers with reference to the centre m is:

$$\vec{a} = (-\mathbf{n1} + \mathbf{n2} + \mathbf{n3})\frac{S}{2} + \vec{m} \tag{10}$$

$$\vec{b} = (\mathbf{n1} + \mathbf{n2} + \mathbf{n3})\frac{S}{2} + \vec{m} \tag{11}$$

$$\vec{c} = (\mathbf{n1} - \mathbf{n2} - \mathbf{n3})\frac{S}{2} + \vec{m} \tag{12}$$

and the sum of squared distance between the tracked corners and their associated desired vertexes of the cube is:

$$y = f(\vec{a},\vec{b},\vec{c}) \equiv |\vec{a} - \vec{a}_T|^2 + |\vec{b} - \vec{b}_T|^2 + |\vec{c} - \vec{c}_T|^2 \tag{13}$$

where $a_T$, $b_T$ and $c_T$ are positions determined from Multiple-PEPT. Manipulation of Eqs. (10)–(12) gives

$$y = g(\mathbf{n1}, \mathbf{n2}, \mathbf{n3}) = \left|(-\mathbf{n1}+\mathbf{n2}+\mathbf{n3})\frac{s}{2}+m-\vec{a}_T\right|^2 + \left|(\mathbf{n1}+\mathbf{n2}+\mathbf{n3})\frac{s}{2}+m-\vec{b}_T\right|^2 + \left|(\mathbf{n1}-\mathbf{n2}-\mathbf{n3})\frac{s}{2}+m-\vec{c}_T\right|^2 \quad (14)$$

Therefore, the vectors **n1**, **n2** and **n3** can be obtained by the minimization of (14). The coordinates of *a*, *b* and *c* can be obtained from (10)–(12), allowing the other coordinates to be reconstructed.

### 3.3. Reconstruction of the solid rotational motion in a three-dimensional space

From Fig. 2C, the velocity of "a" relative to "m" (Smith and Smith, 2000) is

$$\dot{\mathbf{r}}_a = \mathbf{u}_a \times \mathbf{r}_a \quad (15)$$

where $\mathbf{u}_a$ is angular velocity, and $\mathbf{u}_a = (\omega_x, \omega_y, \omega_z)$.

The actual velocity of "a" will therefore be

$$\dot{\mathbf{R}}_a = \dot{\mathbf{R}}_m + \mathbf{u}_a \times \mathbf{r}_a \quad (16)$$

Thus

$$\mathbf{V}_a = \mathbf{V}_m + \mathbf{u}_a \times (\vec{a} - \vec{m}) \quad (17)$$

In a similar way,

$$\mathbf{V}_b = \mathbf{V}_m + \mathbf{u}_b \times (\vec{b} - \vec{m}) \quad (18)$$

$$\mathbf{V}_c = \mathbf{V}_m + \mathbf{u}_c \times (\vec{c} - \vec{m}) \quad (19)$$

The velocity is calculated by three successive locations as follows.

$$V_x(t_i) = \frac{1}{2}\left(\frac{x(t_{i+1}) - x(t_i)}{t_{i+1} - t_i} + \frac{x(t_i) - x(t_{i-1})}{t_i - t_{i-1}}\right) \quad (20)$$

In a similar way, the velocity in *y* and *z* directions can be obtained.

For a rigid body, the angular velocity of any point in the rigid body round the mass-centre should be same, and described by $\boldsymbol{\omega}$.

If a function of $\boldsymbol{\omega}$ is defined as follows:

$$y = f(\omega) \equiv |\mathbf{V}_a - \mathbf{V}_m - \boldsymbol{\omega} \times (\vec{a} - \vec{m})|^2 + |\mathbf{V}_b - \mathbf{V}_m - \boldsymbol{\omega} \times (\vec{b} - \vec{m})|^2 + |\mathbf{V}_c - \mathbf{V}_m - \boldsymbol{\omega} \times (\vec{c} - \vec{m})|^2 \quad (21)$$

the $\boldsymbol{\omega}$ can be calculated by the minimization of (21).

Then the observed internal spin rate of the solid can be calculated as in Eq. (22).

$$N = \frac{|\boldsymbol{\omega}|}{2\pi} \quad (22)$$

## 4. Tests of reconstruction of translational and rotational motions

To validate the applicability of Multiple-PEPT, a set of experiments were performed by tracking a cube with a dimension of 12 mm. The cube was mounted on a turntable rotating at a constant speed for each run approximately at the centre of the field of view of the detectors, and three tracers were placed at the corners *a*, *b* and *c* of the cube, as shown in Fig. 3. The data collection was taken 30 min for each run. The rotating speeds of the turntable varied from 3 rpm (=0.314 radians/s) to 48 rpm (=5.023 radians/s) at a radius of 50 mm; and the cube speeds varied from 15.7 mm/s to 250 mm/s. The tracers were labelled by $^{18}$F with different radioactivity initially: Tracer *a*: 326 μCi, Tracer *b*: 198 μCi, and Tracer *c*: 97 μCi.

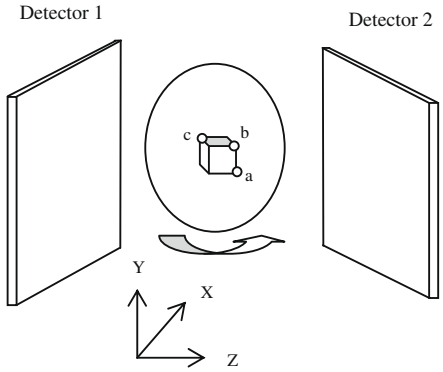


**Fig. 3.** Schematic diagram of Multiple-PEPT for 3-moving-tracer.

The accuracy of the reconstruction of translational and rotational motions was evaluated by the reconstructed translational location and speed errors, and angular speed error in the results as follows.

$$\text{r.m.s. location error}_m \equiv \tilde{p}_m = \sqrt{\frac{\sum_{i=1}^{N}((\hat{x}_m^i - x_m^i)^2 + (\hat{y}_m^i - y_m^i)^2 + (\hat{z}_m^i - z_m^i)^2)}{N}} \quad (23)$$

$$\text{r.m.s. speed error}_m \equiv \tilde{v}_m = \sqrt{\frac{\sum_{i=1}^{N}((\hat{v}x_m^i - vx_m^i)^2 + (\hat{v}y_m^i - vy_m^i)^2 + (\hat{v}z_m^i - vz_m^i)^2)}{N}} \quad (24)$$

$$\text{r.m.s. angular speed error} \equiv \tilde{\omega} = \sqrt{\frac{\sum_{i=1}^{N}((\hat{\omega}_x^i - \omega_x^i)^2 + (\hat{\omega}_y^i - \omega_y^i)^2 + (\hat{\omega}_z^i - \omega_z^i)^2)}{N}} \quad (25)$$

where $\hat{x}_k^i$ is the estimated position of solid at the centre *m* in *x*-direction at time *i*; the actual value is $x_k^i$.

Both translational and rotational motions reconstructed by tracking three particles are similar for all tests and thus this paper only shows one example for the three particles on a turntable rotating at 48 rpm round *x*-axis in the *xyz* space. The translational motion location and velocity, and angular velocity are shown in Figs. 4–6, respectively. The test results of translational location, translational speed and angular speed errors are shown in Fig. 7A–D.

The turntable for the given example rotated the *x*-axis in the *xyz* space, it means that the turntable rotated in the *y*–*z* plane with a constant position in *x*-direction. As well expected, the position in *x*-direction was almost constant (about 0 ± 1 mm) which had a very good agreement with the theoretical value of 0 mm; and the *y* and *z* position coordinates were periodic functions of time differing by a quarter of one period, as shown in Fig. 4. Similarly, the velocity in *x*-direction was almost constant (about 0 ± 4 mm/s) which were very close to the theoretical value of 0 mm/s; and the velocity components in *y*- and *z*-direction were periodic functions of time differing by a quarter of one period, as shown in Fig. 5. The angular velocity component was significant only in the *x*-direction, about 5.023 ± 0.5 radians/s while those in other directions were about 0 ± 0.5 radians/s, which matched well with

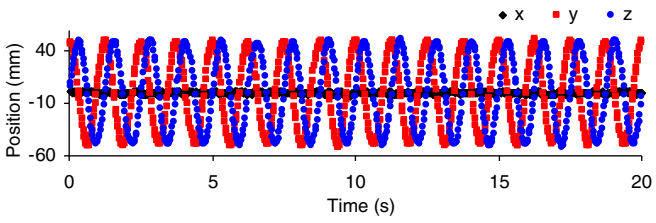


**Fig. 4.** Part of translational location data from Multiple-PEPT.

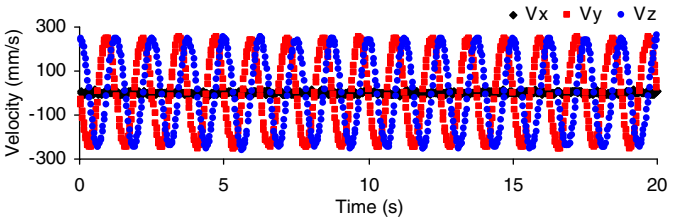


**Fig. 5.** Part of translational velocity data from Multiple-PEPT.

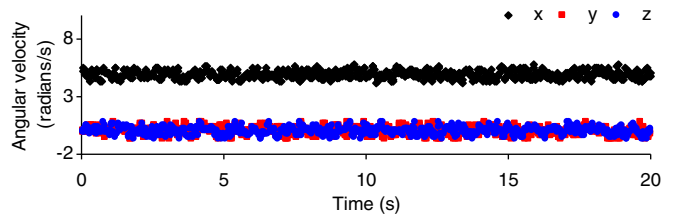


**Fig. 6.** Part of angular velocity data from Multiple-PEPT.

the theoretical values of 5.023 and 0 radians/s, respectively, as shown in Fig. 6.

Fig. 7 shows that the errors of location and speed increased as the cube speed increased. However, the r.m.s. translational location error were less than 4 mm; and the r.m.s. translational and angular speeds errors were less than 10% and 23%, respectively, when the translational and angular speeds of the cube were up to 250 mm/s and 48 rpm, respectively. The results show that the errors are acceptable to most engineering applications. It means that Multiple-PEPT can be used to study both translational and rotational motions of the solids.

To demonstrate that the three dimensional image of the cube can be reconstructed at any time by Multiple-PEPT, part of the trajectory of the spinning cube is shown in Fig. 8, which uses the same data as Fig. 4. The cubes were pictured at regular intervals of 0.125 s for a 1.25 s period.

## 5. An example of application to a rotating can

To demonstrate the applicability of Multiple-PEPT to elucidate transport phenomena in a realistic engineering system, experiments similar to those in Yang et al. (2008) tracking 3 tracers are performed.

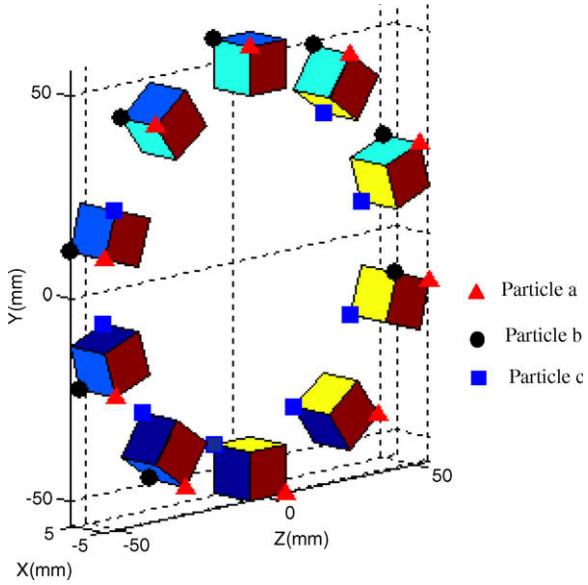


**Fig. 8.** Part of spinning cubes from Multiple-PEPT over a 1.25 s period.

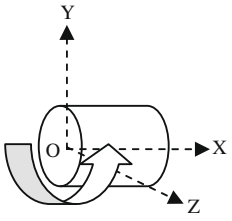


**Fig. 9.** Geometry of the rotating can in three-dimensional space.

The cans had a height of 119 mm and diameter of 100 mm and were supplied by Stratford Foods. The experiments were designed to observe the effect of solids fraction on solids rotational and translational motions. The liquid used was water. The experiments were carried out at three solids fractions, which were 10%, 20% and 40% (v/v). The solids used were cubed potatoes with a dimension of

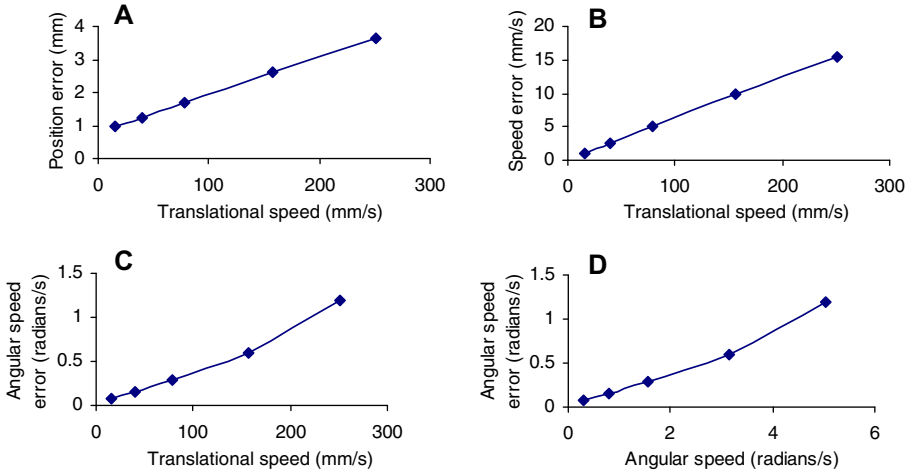


**Fig. 7.** Tracked errors: (A) translational position error; (B) translational speed error; (C) estimated angular speed error as a function of translational speed; (D) estimated angular speed error as a function of angular speed.

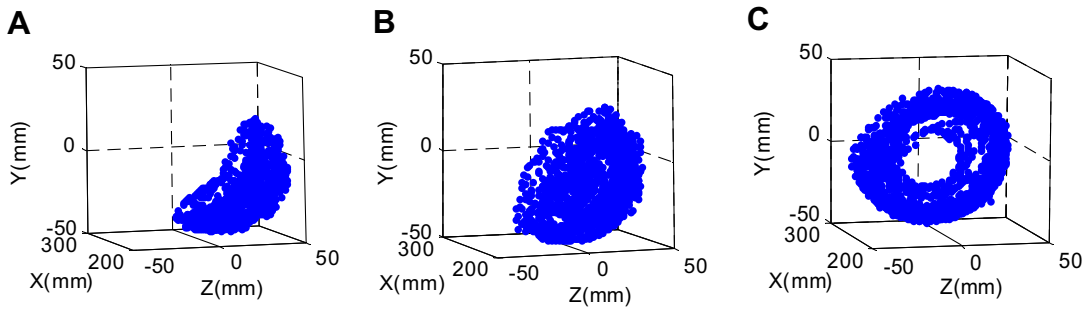


**Fig. 10.** Solids trajectories over a 2 min period: (A) 10% solids; (B) 20% solids; (C) 40% solids.

approximate 12 mm and density 1.08 kg/L. For each run, a headspace (fraction of air in the can) of 10% was used and the experiment was run for 20 min. The cans were rotated on a horizontal tube roller at 12 rpm anticlockwise, as shown in Fig. 9. The three tracers had iso-density with respect to the cubed potato, were initially labelled with radioactivity: 625 μCi, 420 μCi and 238 μCi, respectively, and mounted at the three vertices of a cubed potato, as shown in Fig. 2A. The size of tracers was less than 0.5 mm; their influence on the solids motions was negligible. All experiments were performed at the ambient temperature.

To make sure that the experimental runs were valid, the shape of potatoes was checked before and after each run. There was no deformation through the whole experiment.

### 5.1. Effect of solids fraction on solids trajectories

Fig. 10A–C shows the part of trajectories of the cubed potatoes over a 2 min period, with the solids fractions of 10%, 20% and 40%, respectively. The results show that the solids moving pattern within the can varied significantly with the solids fraction.

The solids trajectories show a "D" shape with the flat line faced to the headspace, probably due to the effect of the headspace on the flow fluids. Similar D shape paths were found by Bakalis et al. (2006) for the flow of viscous fluids, by Ding et al. (2002) for granular motion in rotating drums, and by Yang et al. (2008) for solids flow in a rotating can. The shape changes with the solids fraction, as shown in Fig. 10. With the can rotated anticlockwise, the solids sit on the right-side wall which rotated upwards. The right-side wall applies drag to the solids near the can wall. As described in Yang et al. (2008) and Ding et al. (2002), the solids within the can can be divided into two layers, namely, a 'passive' layer where solids are carried up by the can wall, and an 'active' layer where solids cascade down. The passive layer is adjacent to the right-side wall, where solids move almost as a packed rigid body, following the can's rotation at slightly slower speed. At some point the gravitation dominates the drag force. The solids move down over the passive layer, forming an active layer, where solids do not move as a rigid body and a large radial displacement can be observed. The falling trajectories in the active layer were dependent on the solids fraction within the can, closer to the left-side wall with increasing solids fraction. As shown in Fig. 10B, the solids fraction of 20% gave a much thicker active layer, and a large radial displacement than the other two solids fractions. However, at 40%, solids move almost as a rigid body following the rotating can probably due to the high solid fraction, resulting in a limited motion for the solids.

### 5.2. Distribution of solids residence time and solids exchange frequency from the wall to the centre of the can

Solids residence time means the amount of time spent by the solid within a particular region from the side view of *YOZ* plane.

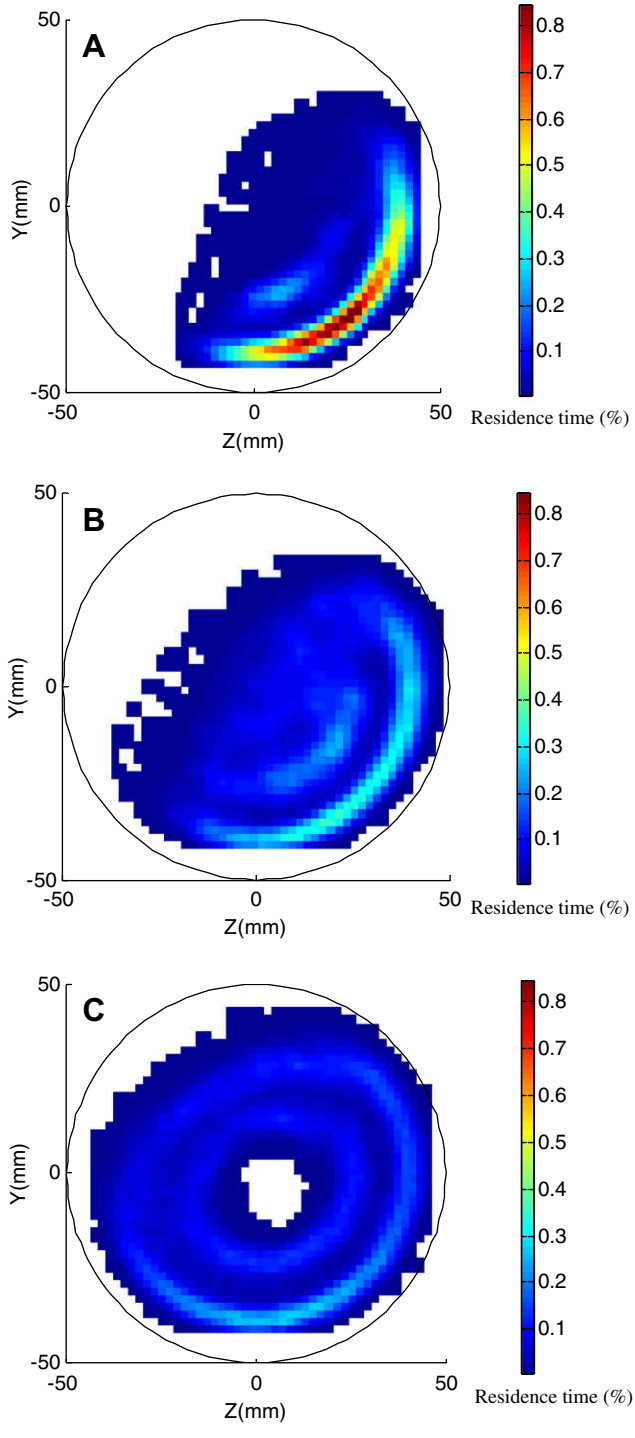


**Fig. 11.** Distribution of solids residence time: (A) 10% solids; (B) 20% solids; (C) 40% solids.

The number of occurrences of a solid traveling from the wall to the centre of the can per second is defined as the solid exchange frequency. Thus, the contribution of solids motion to the convective heat transfer during the can heating can be qualitatively indicated by the residence time map and solids exchange frequency from the wall to the central region of the can. Fig. 11 shows the effect of solids fraction on the distribution of solids residence time. Fig. 12 shows the distribution of solids residence time in different sections. Fig. 13 shows the effect of solids fraction on the exchange frequency from the wall to the central region of the can. The results indicate that the residence time and the exchange frequency varied significantly with the solids fraction. Solids spent longer time in the passive layer (on the rising wall), but less time in the central region, particularly for the solids fraction of 10% and 40% as shown in Figs. 11 and 12. The exchange of solids from the wall to the central region was best when the solids fraction was about 20% (Fig. 11B) or somewhere between 20% and 40%. It also can be seen from Fig. 13. The solids exchange frequency was 0.15 Hz for the solids fraction of 20%, while it was 0.00083 Hz for the solids fractions up to 40%. However, it is also interesting to note that the uniformity of solids residence time distribution increased with solids fraction from Figs. 11 and 12. The rotating solids ring might act as a scraper reducing the boundary layer at the inner wall and enhancing heat transfer.

### 5.3. Effect of solids fraction on internal spin of solids

To find how the internal spin of solids varies with the solids position, the can was divided by several 2 mm × 2 mm × 119 mm cuboids, the solids spin rate was calculated by using their average for those solids whose the centres lay with in the cuboid. Thus, the average solids spin rate $\overline{N}$ was given by

$$\overline{N}_j = \frac{1}{l}\sum_{i=1}^{l} N(j,i) \tag{26}$$

where $N(j,i)$ denoted the instantaneous spin rate for the $i$th position of solid in the $j$th cuboid.

The statistics of the internal spin rate of solids for (i) average of spin rate ($\mu$) and (ii) the standard deviation of spin rate ($\sigma$), were obtained by the following equations:

$$\mu = \frac{1}{k}\sum_{j=1}^{k} \overline{N}_j \tag{27}$$

$$\sigma = \sqrt{\frac{\sum_{j=1}^{k}(\overline{N}_j - \mu)^2}{k}} \tag{28}$$

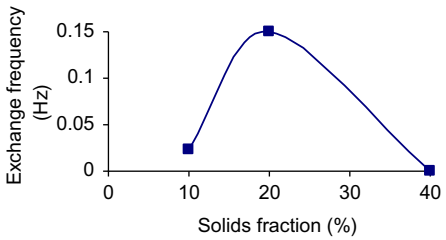


**Fig. 13.** Solids exchange frequency from the wall to the central region of the can as a function of the solids fraction.

Fig. 14A–C show the internal spin rate of solids from the side view of *YOZ* plane over a 20 min period under the same experimental conditions as described above. To minimise of the influence of outliers, only the central 90% of data for the internal spin rate around the average were used in Fig. 15, supposing that the internal spin rate is normally distributed. Table 1 shows the parameters for the spin rate, calculated from Eqs. (27) and (28).

The internal spin rate in Fig. 15 was calculated within 1.6 standard deviations of the average from Table 1 for the 90% as the probability of a internal spin rate of $X$, within 1.6 standard deviations of the average, is 90% for a normal distribution (Canavos, 1984), as shown in Eq. (29).

$$P(\mu - 1.6\sigma \leqslant X \leqslant \mu + 1.6\sigma) = \frac{1}{\sqrt{2\pi}}\int_{-1.6}^{1.6} \exp(-z^2/2)\,dz = 0.9 \tag{29}$$

where $P$ is a function of probability, $\mu$ is the average of the internal spin rate, and $\sigma$ is the standard deviation of spin rate.

As expected, the solids spin is related to the flow pattern of the bulk solids. When the can was rotated in an anticlockwise direction, the passive layer was located adjacent to the right-side wall. Within this layer, solids spin was limited. The internal spin rate was much more uniform and lower than that in the active layer as shown in Fig. 14. In contrast, in the active layer at the left-side of the can, the solids did not move as a rigid body, as shown in Fig. 10A and B. Collision and fast motion of solids result in greater rotation in the active regimes as shown in Fig. 14A–B. With increasing solids fraction, the active regime was shrinking close to the headspace, and the internal spin rate became more uniform and milder within most of the can, except the region close to the headspace, as shown in Fig. 14C.

The range of the internal spin rate decreased with the solids fraction from Fig. 15. The spin rate lay somewhere between (i) 3

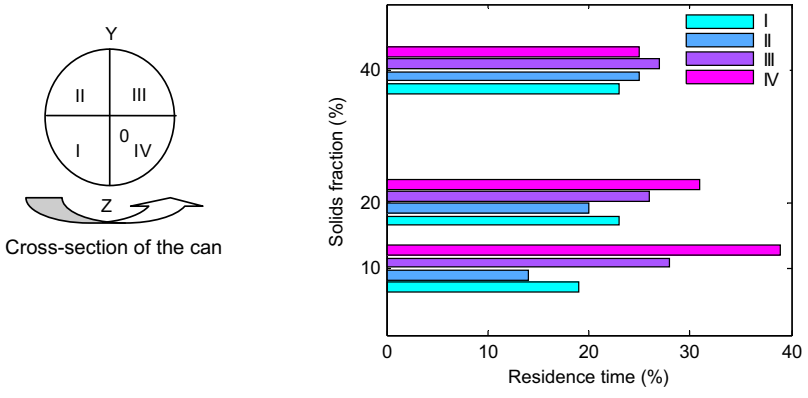


**Fig. 12.** Distribution of solids residence time for the solids in different sections.

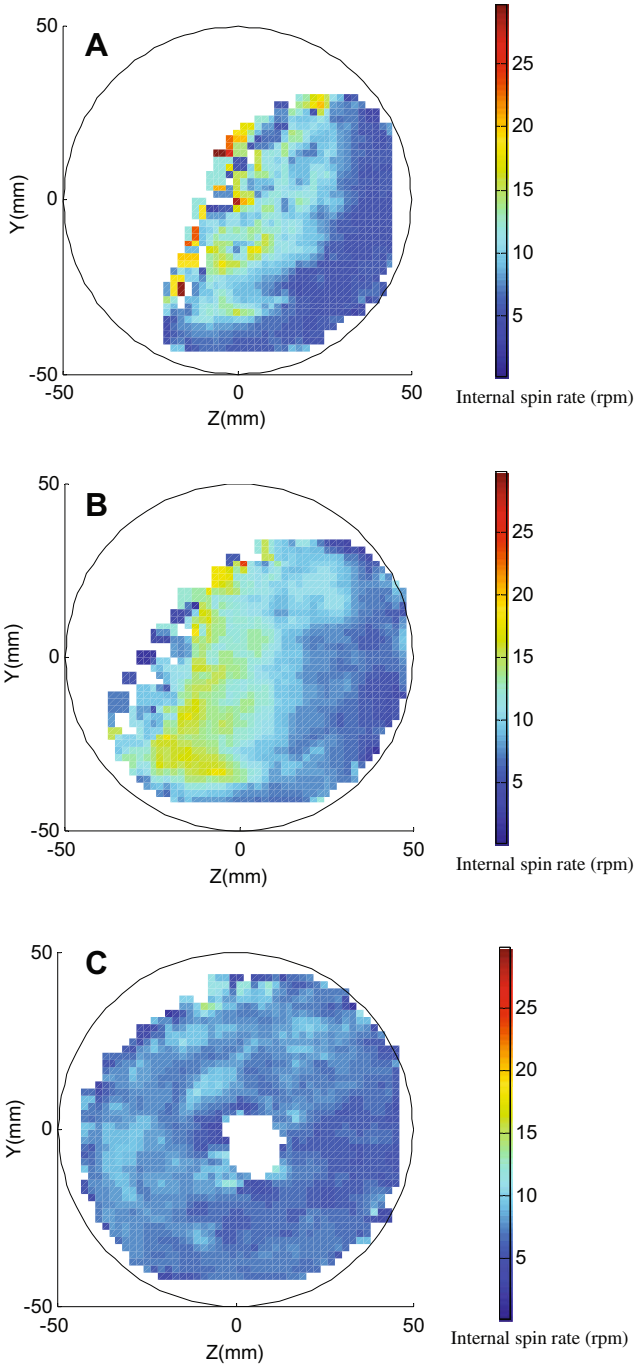


**Fig. 14.** Internal spin rate of solids over a 20 min period: (A) 10% solids; (B) 20% solids; (C) 40% solids.

and 30 rpm when solids fraction was 10%, (ii) 1.8 and 24 rpm for the solids fraction of 20%, and (iii) 1.8 and 14.4 rpm for the solids fraction of 40%. The average decreased about 20% and 29% when the solids fraction was up to 40%, comparing to these with the solids fractions of 10% and 20%, respectively. The results suggest that these changes in solids spin may have a great impact on the flow pattern.

Over all, the internal spin is dependent on the concentration of solids and solids collision, which are related to the flow pattern of the bulk solids. The spin may also have a high influence on the flow pattern.

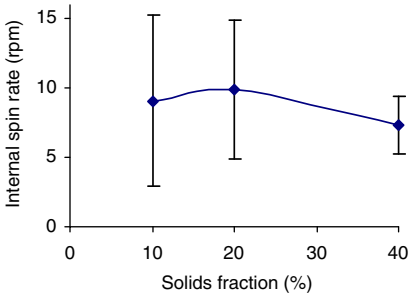


**Fig. 15.** Internal spin rate of solids for 90% of cuboids around the average speed over a 20 min period.

**Table 1**
Statistic parameters for the internal spin rate of solids

| Solids fraction (%) | Max internal spin rate (rpm) | Min internal spin rate (rpm) | $\mu$ Average of internal spin rate (rpm) | $\sigma$ Standard deviation of internal spin rate (rpm) |
|---|---|---|---|---|
| 10 | 30 | 3 | 9.084 | 3.858 |
| 20 | 24 | 1.8 | 9.936 | 3.12 |
| 40 | 14.4 | 1.8 | 7.362 | 1.308 |

To obtain the detail of the solids spin, the cube can be reconstructed at any time through tracking the three labelled tracer particles at the corners of the cube. To demonstrate that the multiple particle tracking technique works, part of the trajectories of the spinning cube is shown in Fig. 16A and B corresponding to the solids fractions of 20% and 40%, respectively. The cubes were pictured 7 times at regular intervals over a circulation period.

## 6. Conclusions

It has been shown that Multiple-PEPT can non-invasively track three particles. It also has been shown that both rotational and translational motions of the solid can be accurately reconstructed through tracking three radioactively labelled tracers mounted to corners of the solid. The errors of estimated location and speed increased with the solid speed. However, the r.m.s. translational location error was less than 4 mm; and the r.m.s. translational and angular speeds errors were less than 10% and 23%, respectively, when the speed was up to 250 mm/s. The errors are acceptable to most engineering applications. Multiple-PEPT can be used to study both translational and rotational motions of solids to further investigate heat transfer and mixing processes.

The example of application to the rotating can system has demonstrated that Multiple-PEPT can provide information on the solids flow pattern, the distribution of solids residence and solids exchange frequency from the wall to the central region of the can, through the reconstruction of the translational motion; in the meantime, it can give information on the internal spin of solids, through the reconstruction of rotational motion; resulting in a better understanding of the phenomena of thermal processes. It has further demonstrated that Multiple-PEPT can be used to track a range of motions of the solid which can be used for fundamental research as well as industrial applications.

## Acknowledgements

The authors gratefully acknowledge financial support from the EPSRC for this work and the Birmingham positron imaging centre.

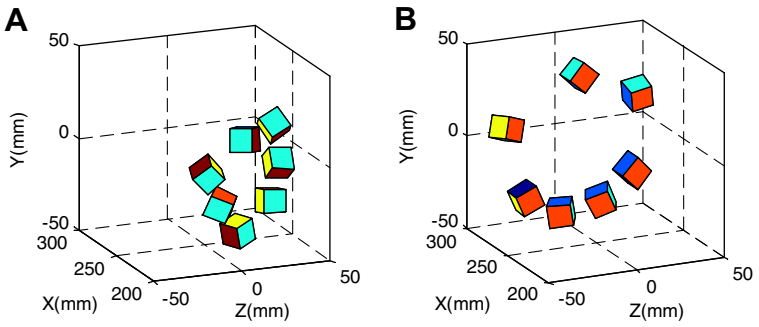


**Fig. 16.** Part of the trajectories of the spinning solids: (A) 20% solids; (B) 40% solids.

## References


Bakalis, S., Cox, P.W., Russell, A.J., Parker, D.J., Fryer, P.J., 2006. Development and use of Positron Emitting Particle Tracking (PEPT) technique for velocity measurements in viscous fluids in pilot scale equipment. Chem. Eng. Sci. 61, 1864–1877.

Barigou, M., Fairhurst, P.G., Fryer, P.J., Pain, J.P., 2003. Concentric flow regime of solid–liquid food suspensions: theory and experiment. Chem. Eng. Sci. 58, 1671–1686.

Bhusarapu, S., Cassanello, M., Al-Dahhan, M.H., Dudukovic, M.P., Trujillo, S., O'Hern, T.J., 2007. Dynamical features of the solid motion in gas–solid risers. Int. J. Multiphase Flow 33, 164–181.

Canavos, G.C., 1984. Applied Probability and Statistical Methods. Little Brown Company Limited, Canada.

Conway, S.L., Lekhal, A., Khinast, J.G., Glasser, B.J., 2005. Granular flow and segregation in four-bladed mixer. Chem. Eng. Sci. 60, 7091–7107.

Ding, Y.L., Forster, R., Seville, J.P.K., Parker, D.J., 2002. Granular motion in rotating drums: bed turnover time and slumping – rolling transition. Powder Technol. 124, 18–27.

Duchanoy, C., Thibauld, R.G., Jongen, T.R.G., 2003. Efficient simulation of liquid–solid flows with high solids fraction in complex geometries. Computers Fluids 32, 1453–1471.

Duursma, G.R., Glass, D.H., Rix, S.J.L., Yorquez-Ramirez, M.I., 2001. PIV investigations of flow structures in the fluidised bed freeboard region. Powder Technol. 120, 2–11.

Fairhurst, P.G., Barigou, M., Fryer, P.J., Pain, J.P., Parker, D.J., 2001. Using positron emission particle tracking (PEPT) to study nearly neutrally buoyant particles in high solid fraction pipe flow. Int. J. Multiphase Flow 27, 1881–1901.

Fan, X., Parker, D.J., Smith, M.D., 2006a. Enhancing $^{18}$F uptake in a single particle for positron emission particle tracking through modification of solid surface chemistry. Nucl. Instrum. Methods Phys. Res. A 558, 542–546.

Fan, X., Parker, D.J., Smith, M.D., 2006b. Labelling a single particle for positron emission particle tracking using direct activation and ion-exchange techniques. Nucl. Instrum. Methods Phys. Res. A 562, 345–350.

Fan, X., Parker, D.J., Yang, Z., Seville, J.P.K., Baeyens, J., 2008a. The effect of bed materials on the solid/bubble motion in a fluidised bed. Chem. Eng. Sci. 63, 943–950.

Fan, X., Yang, Z., Parker, D.J., Armstrong, B., 2008b. Prediction of bubble behaviour in fluidised beds based on solid motion and flow structure. Chem. Eng. J. 140, 358–369.

Gera, D., Gautam, M., Tsuji, Y., Kawaguchi, T., Tanaka, T., 1998. Computer simulation of bubbles in large-particle fluidized beds. Powder Technol. 98, 38–47.

Goldschmidt, M.J.V., Beetstra, R., Kuipers, J.A.M., 2004. Hydrodynamic modelling of dense gas-fluidised beds: comparison and validation of 3D discrete particle and continuum models. Powder Technol. 142, 23–47.

Horio, M., Kuroki, H., 1994. Three-dimensional flow visualization of dilutely dispersed solids in bubbling and circulating fluidized beds. Chem. Eng. Sci. 49, 2413–2421.

Hussainov, M., Kartushinsky, A., Mulgi, A., Rudi, U., 1996. Gas–solid flow with the slip velocity of particles in a horizontal channel. J. Aerosol Sci. 27, 41–59.

Kale, S.R., Ramezan, M., Anderson, R.J., 1989. Measurement of particle rotational velocity using a laser anemometer. Particle Particle Systems Characterization 6, 59–63.

Lareo, C., Branch, C.A., Fryer, P.J., 1997a. Particle velocity profiles for solid–liquid food flows in vertical pipes. Part I: single particles. Powder Technol. 93, 23–34.

Lareo, C., Nedderman, R.M., Fryer, P.J., 1997b. Particle velocity profiles for solid–liquid food flows in vertical pipes, Part II. Multiple particles. Powder Technol. 93, 35–45.

Lee, H.Y., Hsu, I.S., 1996. Particle spinning motion during saltating process. J. Hydraulic Eng. 122, 587–590.

Liu, S., Pain, J.P., Proctor, J.M., de Alwis, A.A.P., Fryer, P.J., 1993. An experimental study of particle flow velocities in solid–liquid food mixtures. Chem. Eng. Commun. 124, 97–114.

Mankad, S., Branch, C.A., Fryer, P.J., 1995. The effect of particle slip on the sterilization of solid–liquid food mixtures. Chem. Eng. Sci. 50, 1323–1336.

Mankad, S., Nixon, K.M., Fryer, P.J., 1997. Measurements of particle-liquid heat transfer in systems of varied solids fraction. J. Food Eng. 31, 9–33.

Mankad, S., Fryer, P.J., 1997. A heterogeneous flow model for the effect of slip and flow velocities on food steriliser design. Chem. Eng. Sci. 52, 1835–1843.

Parker, D.J., Broadbent, C.J., Fowles, P., Hawkesworth, M.R., McNeil, P., 1993. A positron emission particle tracking – a technique for studying flow within engineering equipment. Nucl. Instrum. Methods Phys. Res. A 326, 592–607.

Parker, D.J., Broadbent, C.J., Fowles, P., Hawkesworth, M.R., McNeil, P.A., 1996. Positron emission tomography for process applications. Measurement Sci. Technol. 7, 287–296.

Parker, D.J., Allen, D.A., Benton, D.M., Fowles, P., McNeil, P.A., Tan, M., Beynon, T.D., 1997a. Developments in particle tracking using the Birmingham Positron Camera. Nucl. Instrum. Methods Phys. Res. A 392, 421–426.

Parker, D.J., Dijkstra, A.E., Martin, T.W., Seville, J.P.K., 1997b. Positron emission particle tracking studies of spherical particle motion in rotating drums. Chem. Eng. Sci. 52, 2011–2022.

Parker, D.J., Forster, R.N., Fowles, P., Takhar, P.N., 2002. Positron emission particle tracking using the new Birmingham positron camera. Nucl. Instrum. Methods Phys. Res. A 477, 540–545.

Razzak, S.A., Barghi, S., Zhu, Z.-X., 2007. Electrical resistance tomography for flow characterization of a gas–liquid–solid three-phase circulating fluidized bed. Chem. Eng. Sci. 62, 7253–7263.

Reyes, J.N., Lafi, A.Y., Saloner, D., 1998. The use of MRI to quantify multi-phase flow pattern transitions: an application to horizontal slug flow. Nucl. Eng. Design 184, 213–228.

Santomaso, A., Olivi, M., Canu, P., 2004. Mechanisms of mixing of granular materials in drum mixers under rolling regime. Chem. Eng. Sci. 59, 3269–3280.

Santomaso, A., Olivi, M., Canu, P., 2005. Mixing kinetics of granular materials in drums operated in rolling and cataracting regime. Powder Technol. 152, 41–51.

Smith, P., Smith, R.C., 2000. Mechanics (pp254–269). John Wiley & Sons Ltd., New York.

Tsuji, Y., Morkawa, Y., Mizumo, O., 1985. Experimental measurement of the Magnus force on a rotating sphere at low Reynolds numbers. J. Fluid Eng. 107, 484–488.

Wang, D.G., Sadhal, S.S., Campbell, C.S., 1989. Particle rotation as a heat transfer mechanism. Int. J. Heat Mass Transfer 32, 1413–1423.

Werther, J., 1999. Measurement techniques in fluidized beds. Powder Technol. 102, 15–36.

White, B.R., Schulz, J.C., 1977. Magnus effect in saltation. J. Fluid Mech. 81, 497–512.

White, B.R., 1982. Two-phase measurements of saltating turbulent boundary layer flow. Int. J. Multiphase Flow 8, 459–473.

Yang, Z., Parker, D.J., Fryer, P.J., Bakalis, S., Fan, X., 2006. Multiple-particle tracking – an improvement for positron particle tracking. Nucl. Instrum. Methods Phys. Res. A 564, 332–338.

Yang, Z., Fryer, P.J., Bakalis, S., Fan, X., Parker, D.J., Seville, J.P.K., 2007a. An improved algorithm for tracking multiple, freely moving particles in a Positron Emission Particle Tracking system. Nucl. Instrum. Methods Phys. Res. A 577, 585–594.

Yang, Z., Fan, X., Fryer, P.J., Parker, D.J., Bakalis, S., 2007b. Improved multiple-particle tracking for studying flows in multiphase systems. AIChE J. 53, 1941–1951.

Yang, Z., Fan, X., Bakalis, S., Parker, D.J., Fryer, P.J., 2008. Impact of solids fraction and fluid viscosity on solids flow in rotating cans. Food Res. Int. 41, 658–666.

You, C.F., Qi, H.Y., Xu, X.C., 2001. Numerical simulation of Magnus lift on a coal particle. J. Eng. Thermophys. 22, 625–628.